



OPEN

Behavior and properties of water in silicate melts under deep mantle conditions

Bijaya B. Karki^{1✉}, Dipta B. Ghosh¹ & Shun-ichiro Karato²

Water (H₂O) as one of the most abundant fluids present in Earth plays crucial role in the generation and transport of magmas in the interior. Though hydrous silicate melts have been studied extensively, the experimental data are confined to relatively low pressures and the computational results are still rare. Moreover, these studies imply large differences in the way water influences the physical properties of silicate magmas, such as density and electrical conductivity. Here, we investigate the equation of state, speciation, and transport properties of water dissolved in Mg_{1-x}Fe_xSiO₃ and Mg_{2(1-x)}Fe_{2x}SiO₄ melts (for $x=0$ and 0.25) as well as in its bulk (pure) fluid state over the entire mantle pressure regime at 2000–4000 K using first-principles molecular dynamics. The simulation results allow us to constrain the partial molar volume of the water component in melts along with the molar volume of pure water. The predicted volume of silicate melt + water solution is negative at low pressures and becomes almost zero above 15 GPa. Consequently, the hydrous component tends to lower the melt density to similar extent over much of the mantle pressure regime irrespective of composition. Our results also show that hydrogen diffuses fast in silicate melts and enhances the melt electrical conductivity in a way that differs from electrical conduction in the bulk water. The speciation of the water component varies considerably from the bulk water structure as well. Water is dissolved in melts mostly as hydroxyls at low pressure and as –O–H–O–, –O–H–O–H– and other extended species with increasing pressure. On the other hand, the pure water behaves as a molecular fluid below 15 GPa, gradually becoming a dissociated fluid with further compression. On the basis of modeled density and conductivity results, we suggest that partial melts containing a few percent of water may be gravitationally trapped both above and below the upper mantle-transition region. Moreover, such hydrous melts can give rise to detectable electrical conductance by means of electromagnetic sounding observations.

Although the majority of water in the Earth's mantle is in minerals, water in silicate melts also plays a key role in global water cycle^{1–3}. During the accretion state, large-scale magma ocean may have served as a reservoir of volatiles including water delivered to Earth. In the later stages of Earth evolution, melting is limited, mostly existing as partial melts in regions below mid-ocean ridges, regions above and below the mantle-transition region, and atop the core-mantle boundary. These hydrous silicate magmas are thus important in controlling the storage and transport of water in the interior³.

Water dissolved in silicate melts can significantly influence the host physical properties, for instance, by lowering the density and enhancing the electrical conductivity^{4–9}. One of the major goals is to constrain the partial molar volume of water in silicate melts as a function of pressure, temperature, and composition^{6,7,10,11}. This is important in evaluating the density of melts for different water contents at relevant conditions of the Earth's interior. It is the density of silicate melts relative to the density of the surrounding mantle rocks that determines the direction and rate of melt migration and the amount of melt when partial melting occurs at a depth^{12,13}. The melt-crystal density crossover may have played a crucial role in the processes that governed the fractional crystallization and chemical differentiation of early magma oceans as well as in the large fraction of geological history^{3,14,15}. Like the density, the electrical conductivity of silicate melts can be compared with magnetotelluric survey data to detect and quantify possible partial melts in the mantle^{16–18}.

A large number of experimental data is available for hydrous silicate melts at upper mantle-transition zone conditions as recently reviewed by Manning¹⁹. For instance, the measured data at pressures up to 20 GPa in the

¹School of Electrical Engineering and Computer Science, Department of Geology and Geophysics, Center for Computation and Technology, Louisiana State University, Baton Rouge, LA 70803, USA. ²Department of Earth and Planetary Sciences, Yale University, New Haven, CT 06520, USA. ✉email: bbkarki@lsu.edu

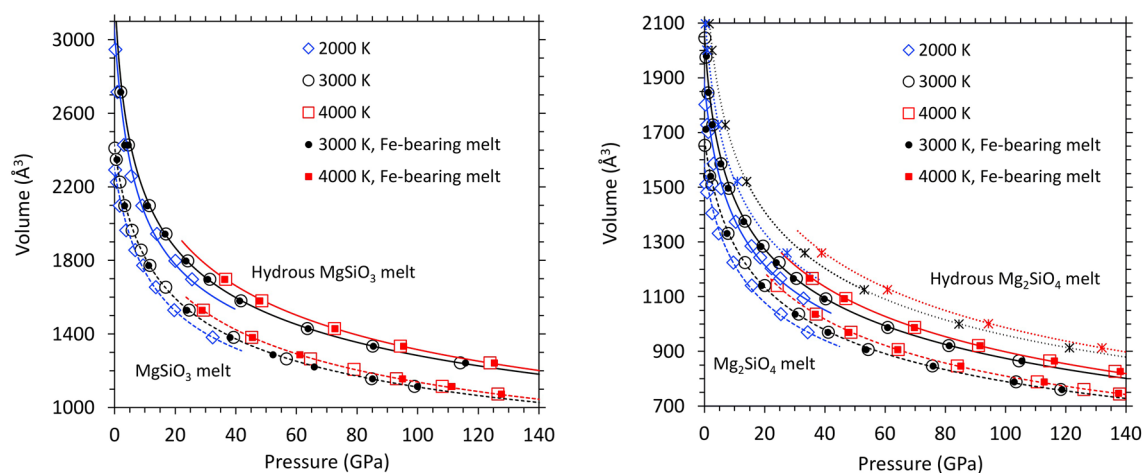


Figure 1. The volume–pressure profiles of hydrous MgSiO_3 (left) and Mg_2SiO_4 (right) melts compared to their dry counterparts at 2000 K (blue diamonds), 3000 K (black circles) and 4000 K (red squares). Curves represent the equation of state fits using Eqs. (1) and (2). The supercells consist of $32\text{MgSiO}_3 + 16\text{H}_2\text{O}$ (8.2 wt% water) and $16\text{Mg}_2\text{SiO}_4 + 8\text{H}_2\text{O}$ (6.0 wt% water) and corresponding iron-bearing phases at 3000 and 4000 K (small solid symbols). Also shown are the results for $16\text{Mg}_2\text{SiO}_4 + 16\text{H}_2\text{O}$ (11.4 wt% water) at three temperatures (asterisks and dotted curves). The errors in the calculated pressure are within the size of symbols.

temperature range 1273–2473 K have recently been used to derive the equation of state for the partial molar volume of water ($\bar{V}_{\text{H}_2\text{O}}$) in magmas¹⁰. While an overall decreasing trend of $\bar{V}_{\text{H}_2\text{O}}$ with pressure is evident, the extent of pressure-induced variations among different measurements and different melt compositions is large and some data even show anomalous increase with compression^{10,20,21}. The measured electrical conductivity data for hydrous silicate melts are rather scarce and scattered^{8,9,22,23}. One primary reason for such inconsistency and difficulty could be associated with the difficulty of quantifying the water content of the samples due to water loss during high temperature experiments.

On the other hand, a relatively few computational studies of hydrous silicate melts have so far been reported using first-principles approach^{6,7,24–26}. These studies have covered relatively high temperatures and chemically simple compositions. Moreover, these computations may have been biased in a quantitative sense. For example, the use of the local density approximation (LDA) for the exchange–correlation functional tends to overbind the structure leading to significant underestimation of the volume⁶. While the calculated partial molar volume of water appears to be mostly insensitive to water concentration²⁶ and melt composition^{6,24,25}, the issue is yet to be fully resolved. Similarly, it is not clear how hydrous contributions to electrical conduction are sensitive to pressure, temperature, and composition.

Here, we evaluate the partial molar volume ($\bar{V}_{\text{H}_2\text{O}}$), speciation, and diffusion coefficients (and the contributions to electrical conductivity) of the water component by performing first-principles molecular dynamics (FPMD) simulations of hydrous $\text{Mg}_{1-x}\text{Fe}_x\text{SiO}_3$ and $\text{Mg}_{2(1-x)}\text{Fe}_{2x}\text{SiO}_4$ liquids for $x=0$ and 0.25 within the generalized gradients approximation (GGA) as in our recent study²⁵. GGA is generally considered to be more accurate than LDA in dealing with hydrous systems. These melt systems differ in the degree of structural polymerization with (Mg + Fe)/Si ratio of 1 and 2. We consider three different concentrations of water (6.0, 8.2, and 11.4 wt%) and wide ranges of pressure (0–140 GPa) and temperature (2000 to 4000 K). We can use the calculated properties of bulk (pure) liquid water as a basis to ascertain the effects of water on melt properties. For instance, the molar volume of water, $V_{\text{H}_2\text{O}}$, may be taken as an upper bound on $\bar{V}_{\text{H}_2\text{O}}$. The high-pressure behavior of water is also crucial to our understanding of giant planets^{27,28} and shock wave data²⁹. The pressure and temperature space considered here covers the phase transition of water from a molecular liquid to a dissociated liquid³⁰. Finally, we use the simulated results to model the effects of water on the density and electrical conductivity of silicate melts and discuss their geophysical implications.

Results and analysis

Equation of state of hydrous silicate melts and pure water. We present the calculated pressure–volume–temperature (P – V – T) results for all hydrous and dry $\text{Mg}_{1-x}\text{Fe}_x\text{SiO}_3$ and $\text{Mg}_{2(1-x)}\text{Fe}_{2x}\text{SiO}_4$ melts for $x=0$ and 0.25 in Fig. 1. The volume of hydrous melts is systematically larger than the volume of the corresponding water-free melts for the supercells used. Our simulations cover the pressure ranges 0 to ~30 GPa at 2000 K, 0 to ~115 GPa at 3000 K, and ~35 to ~140 GPa at 4000 K. In the overlapping pressure regimes, the volume at a higher temperature is larger than the volume at a lower temperature. The calculated results can be adequately represented using the following relation^{7,13}.

$$P(V, T) = P(V, T_0) + B_{TH}(V)(T - T_0) \quad (1)$$

Here, the reference isotherm, $P(V, T_0)$ with $T_0 = 3000$ K, is described by the 4th order Birch–Murnaghan equation with fit parameters shown in Table 1. Hydrous melts have relatively small zero-pressure bulk moduli,

	Hydrous MgSiO ₃	Dry MgSiO ₃	Hydrous Mg ₂ SiO ₄	Dry Mg ₂ SiO ₄
V ₀ (Å ³)	3280 ± 25	2415 ± 16	2050 ± 21 (2370 ± 20)	1670 ± 14
ρ ₀ (g/cm ³) Fe-bearing melt	1.772 1.900	2.209 2.382	1.940 (1.779) 2.144	2.238 2.489
K ₀ (GPa)	8.2 ± 0.5	19.1 ± 1.0	11.3 ± 1.1 (10.1 ± 0.7)	22.2 ± 1.4
K ₀ '	4.85 ± 0.09	4.02 ± 0.13	5.53 ± 0.26 (5.01 ± 0.15)	3.94 ± 0.11
K ₀ ''(GPa ⁻¹)	-0.50 ± 0.07	-0.08 ± 0.02	-0.69 ± 0.16 (-0.53 ± 0.10)	-0.06 ± 0.01
a	26.9	32.7	19.9	7.9
b	-53.8	-70.9	-41.6	-23.4
c	34.0	49.3	28.2	21.1
d	-6.1	-9.9	-5.2	-4.5

Table 1. Equation of state parameters of hydrous and dry silicate melts at 3000 K. The same parameters with higher zero-pressure density as shown apply to their Fe-bearing counterparts. The parameters for melt containing 11.4 wt% water are given in the parentheses.

meaning that they are highly compressible at low pressures. The pressure–volume isotherms become nearly parallel with those of dry melts at high pressure. The thermal pressure coefficient in Eq. 1 is expressed by

$$B_{\text{TH}}(V) = \frac{1}{1000} \left[a + b \left(\frac{V_0}{V} \right) + c \left(\frac{V_0}{V} \right)^2 + d \left(\frac{V_0}{V} \right)^3 \right] \quad (2)$$

where V_0 is the volume at zero pressure and 3000 K (Table 1). Our calculated P – V – T results can be also described by an alternative form for the equation of state, which is based on the hard-sphere model³¹ (Supplementary Text 1). Two forms of equation of state agree well within the interpolation pressure regime at a given temperature, however, they tend to differ considerably at extrapolated pressures (Supplementary Fig. S1).

While the effects of iron (with no spin state) on volume are almost negligible (Fig. 1), iron increases the melt density considerably for mass reason. Iron increases the melt density by about 7.9 and 11.2%, respectively, for Mg_{0.75}Fe_{0.25}SiO₃ and Mg_{1.5}Fe_{0.5}SiO₄ melts uniformly at all pressures along each isotherm (Table 1 and supplementary Fig. 2). The hydrous component, however, decreases the density much more at low pressures. The hydrous effects get rapidly diminished with increasing pressure and become gradual over much of the pressure regime (Supplementary Fig. S2). Our comparison with the measured data of silicate melts shows that GGA systematically underestimates the melt density. For instance, the calculated zero-pressure density is 2.370 g/cm³ compared to the experimental value of 2.583 g/cm³ for MgSiO₃ melt at 1830 K and is 2.394 g/cm³ compared to the experimental value of 2.686 g/cm³ for Mg₂SiO₄ at 2163 K. On the other hand, LDA tends to overestimate the melt density. Nevertheless, the calculated effects of water and iron on the melt density are expected to be comparable between the two types of calculations.

We represent the pressure–volume–temperature results of pure water (Fig. 2) with Eq. 1 by adding a constant pressure term ($P_0 = 0.5$ GPa) for the reference 2000 K isotherm (Table 2). The volume-dependent thermal pressure coefficient is given by $B_{\text{TH}}(V) = -0.92 + 1.2 \left(\frac{V_0}{V} \right) + 0.07 \left(\frac{V_0}{V} \right)^2$ in the units of mPa/K, where V_0 is volume at P_0 . Pure water is extremely compressible as reflected by its unusually small bulk modulus. For instance, the volume along the 2000 K isotherm decreases from 39 cm³ mol⁻¹ at 0.5 GPa to 16 cm³ mol⁻¹ at 5 GPa. It changes more gradually as the fluid is compressed further. Different isotherms tend to become parallel and remain close to each other at high pressures. The calculated volume remains above 5.5 cm³ mol⁻¹ at 150 GPa. Our pressure–volume results at 1000 and 2000 K are similar to the previous calculations which used GGA and relatively large supercells³². The experimentally inferred data on liquid water are confined to low pressures and low temperatures^{33–35}. Our comparisons with the experimental data indicate that GGA overestimates the volume (lying within 5%) whereas LDA underestimates the volume (differing by up to 15%) as shown in Fig. 2. A similar degree of volume overestimation and hence density underestimation by GGA was predicted³² for the 300 K isotherm of ice VII/X compared to the measured data over much wider pressure range up to 126 GPa^{29,36}.

Partial molar volume of dissolved water. We evaluate the partial molar volume of water in silicate melt ($\bar{V}_{\text{H}_2\text{O}}$) from the direct volume difference between hydrous melt ($V_{\text{hydromelt}}$) and dry melt (V_{melt}):

$$\bar{V}_{\text{H}_2\text{O}}(P, T) = (V_{\text{hydromelt}}(P, T) - V_{\text{melt}}(P, T))N_A/n \quad (3)$$

where n is the number of H₂O units in the supercell and N_A is the Avogadro's number. Figure 3 shows the calculated partial molar volume of water in hydrous MgSiO₃ and Mg₂SiO₄ melts and in their iron-bearing phases. We model the compression behavior of $\bar{V}_{\text{H}_2\text{O}}$ using Eq. (1). The reference isotherm $P(V, T_0)$ with $T_0 = 2000$ K considering all results for three iron-free melts (Fig. 3, left) is described by the 4th order Birch–Murnaghan equation of state (Table 2). The zero-pressure bulk modulus is small, consistent with experimentally inferred

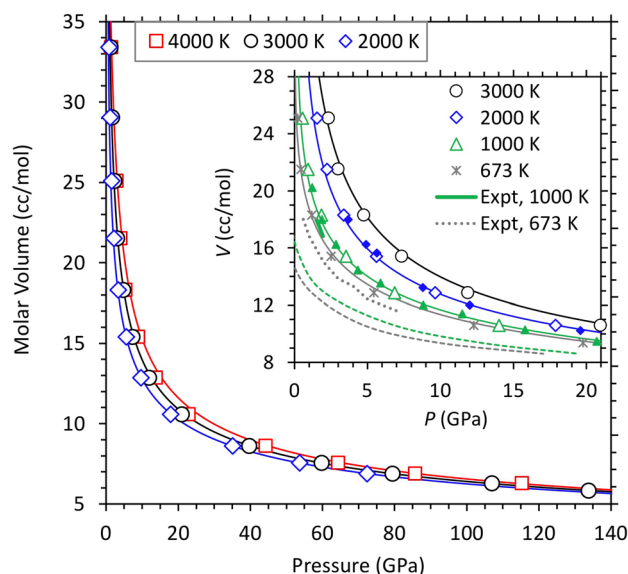


Figure 2. Volume-pressure relationships of pure liquid water at 2000, 3000, and 4000 K. Symbols represent the calculated values and curves represent the corresponding equation of state fits. The inset compares our calculated results (symbols and curves) with the available low-pressure experimental data at 673 and 973 K^{34,35} and the previous calculations shown by small solid triangles and diamonds³². Also shown are the LDA results at 673 and 1000 K (green and gray dashed lines) which are shifted downward with respect to both the GGA and experimental results. The errors in the calculated pressure are within the size of the symbols.

	Water in silicate melts		Pure Water
	Calc	Expt	Calc
T_0 (K)	2000	2000 (1273)	2000
V_0 (cm ³ /mol)	25.0 ± 0.6	35.5 (23.8)	39.0 ± 1.5
K_0 (GPa)	1.91 ± 0.28	1.23 (1.18)	0.72 ± 0.10
K'_0	5.80 ± 0.23	3.31 (3.35)	4.13 ± 0.05
K''_0 (GPa ⁻¹)	-5.1 ± 1.5	-2.81 (-2.95)	-5.2 ± 1.0

Table 2. Equation of state parameters at 2000 K for the water dissolved in silicate melts by considering together the results for all hydrous iron-free melts (MgSiO₃ with 8.2 wt% water, MgSiO₄ with 6.0 and 11.4 wt% water). The experimentally inferred parameters are from Sakamaki¹⁰. The parameters for pure liquid water correspond to a non-zero constant pressure (0.5 GPa).

value¹⁰. The thermal pressure coefficient in the 2000–4000 K range can be described by $B_{TH}(V) = 0.3 - 0.8 \left(\frac{V_0}{V}\right) + 0.9 \left(\frac{V_0}{V}\right)^2$ in the units of mPa/K. For each hydrous silicate melt, \bar{V}_{H_2O} decreases rapidly initially with increasing pressure and then decreases more gradually at higher pressures. Hydrous enstatite melts tend to have larger \bar{V}_{H_2O} than hydrous forsterite melts at pressures close to zero, but they have similar values over much of the pressure regime explored. It is also remarkable that the iron-induced differences in \bar{V}_{H_2O} are negligible at all conditions (Fig. 3, right). Our results thus suggest that the partial molar volume of water remains insensitive to melt composition within the computational uncertainty over almost entire mantle pressure regime (except at low pressures up to 5 GPa).

We compare the calculated \bar{V}_{H_2O} of hydrous melts at 2000 K with the experimental data in the temperature range 1273 to 2473 K at pressures up to 20 GPa in the inset of Fig. 3, left. The experimental melt compositions are more complex, including albite^{37,38}, andesite³⁹, basalt¹², granite⁴⁰, komatiite⁴¹, peridotite⁵, phonolite⁴², rhyolite²⁰, and ultramafic^{4,31}. The reported values at the ambient pressure and 1273 K for \bar{V}_{H_2O} and its temperature derivative ($\partial \bar{V}_{H_2O} / \partial T$) are 22.9 cm³ mol⁻¹ and 9.5 × 10⁻³ cm³ mol⁻¹ K⁻¹, respectively²⁰. More recently reported values²¹ are 23.8 cm³ mol⁻¹ and 15.9 × 10⁻³ cm³ mol⁻¹ K⁻¹. These studies have suggested that the partial molar volume of water is independent of the melt composition and water concentration. Using these two sets of the parameters, we estimate \bar{V}_{H_2O} to be 29.8 and 35.4 cm³ mol⁻¹ at 2000 K and 0 GPa. They are larger than our predicted values of 28.0 cm³ mol⁻¹ for hydrous enstatite melt and 23.5 cm³ mol⁻¹ for hydrous forsterite melt.

Comparison of the calculated partial molar volume of water in silicate melts (\bar{V}_{H_2O}) with the molar volume of pure liquid water (V_{H_2O}) allows us to assess the nature of mixing between the volatile and silicate components. As shown in Fig. 3, \bar{V}_{H_2O} is smaller than V_{H_2O} at zero pressure but the two volumes approach each other rapidly

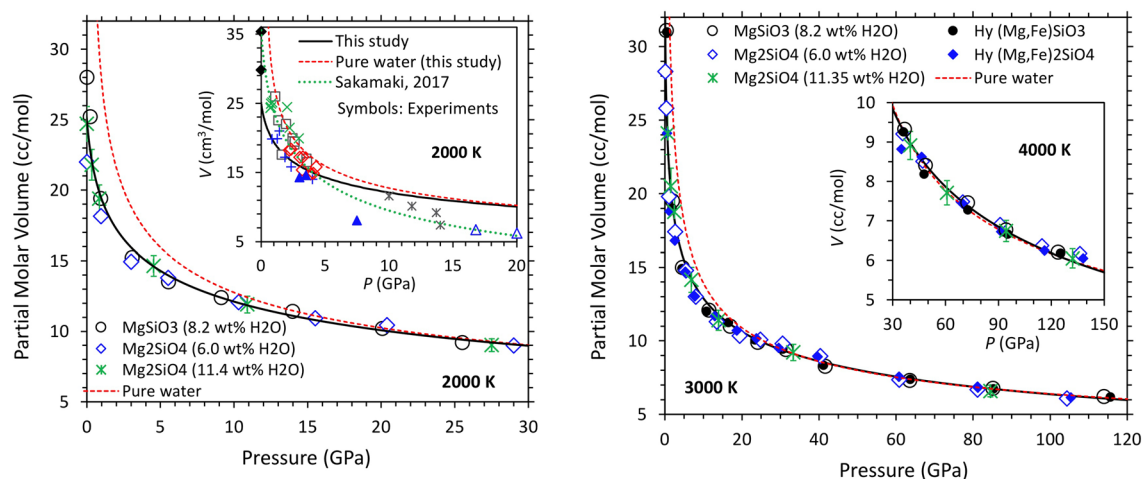


Figure 3. Calculated partial molar volume of water in hydrous MgSiO_3 enstatite melt (circles) and Mg_2SiO_4 forsterite melts (diamonds and asterisks) as a function of pressure at 2000, 3000, and 4000 K and hydrous $\text{Mg}_{0.75}\text{Fe}_{0.25}\text{SiO}_3$ (small solid circles) and $\text{Mg}_{1.5}\text{Fe}_{0.5}\text{SiO}_4$ (small solid diamonds) at 3000 and 4000 K. Also shown is the equation of state fit (solid curve) to all melt results collectively at each temperature in comparison with the calculated equation of state for pure water (this study). The inset on left shows the experimental data on the partial molar volume of water in several silicate melts in the temperature range 1273–2473 K projected to 2000 K using the model of Sakamaki¹⁰. Different symbols represent different melt compositions, plus: andesite³⁹, solid triangle: basalt¹², square: granite⁴⁰, open triangle: komatiite⁴¹, open diamond: peridotite⁵, cross: phonolite⁴², and asterisk: ultramafic^{4,31}; solid diamond: hydrous silicate melts at 0 GPa^{20,21}. The error bars are shown only for the hydrous forsterite results (asterisks) for the sake of clarity.

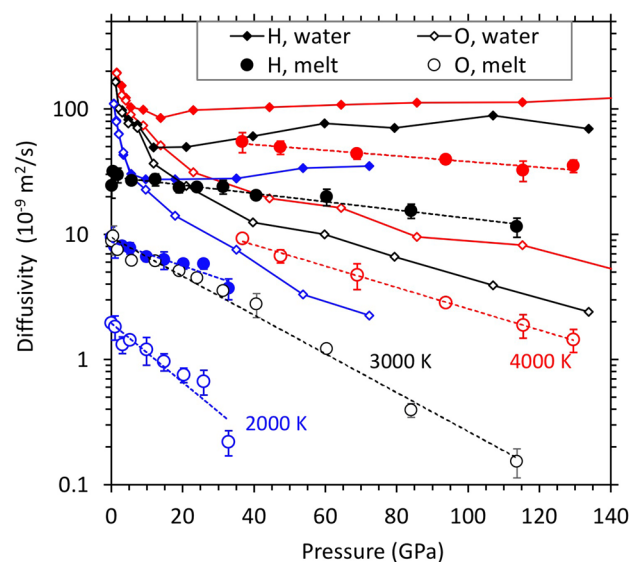


Figure 4. Diffusivity–pressure profiles of hydrogen and oxygen of hydrous silicate melts (symbols) taken as averages over five melt compositions (with the corresponding error bars shown) at three temperatures. Their Arrhenius trends are represented by straight dashed lines. The H and O diffusivity results of pure water are displayed, respectively, as solid and dashed curves (with small symbols). Color encodes temperature: blue 2000 K, black 3000 K, and red 4000 K.

with increasing pressure. The apparent volume of the melt + water solution is large negative ($-18.8 \text{ cm}^3 \text{ mol}^{-1}$ at 0.5 GPa and 2000 K) and remains negative at pressures below 15 GPa, but it becomes almost zero on further compression. The volume of mixing thus changes from non-ideal to ideal with increasing pressure. Non-ideal mixing of silicate melts and H_2O fluid was also implied experimentally at low pressures^{43–45}.

Hydrogen and oxygen diffusion. We find that hydrogen is highly mobile in all melts simulated here, in general agreement with previous computational results^{26,46,47}. At each temperature, the diffusivity decreases with

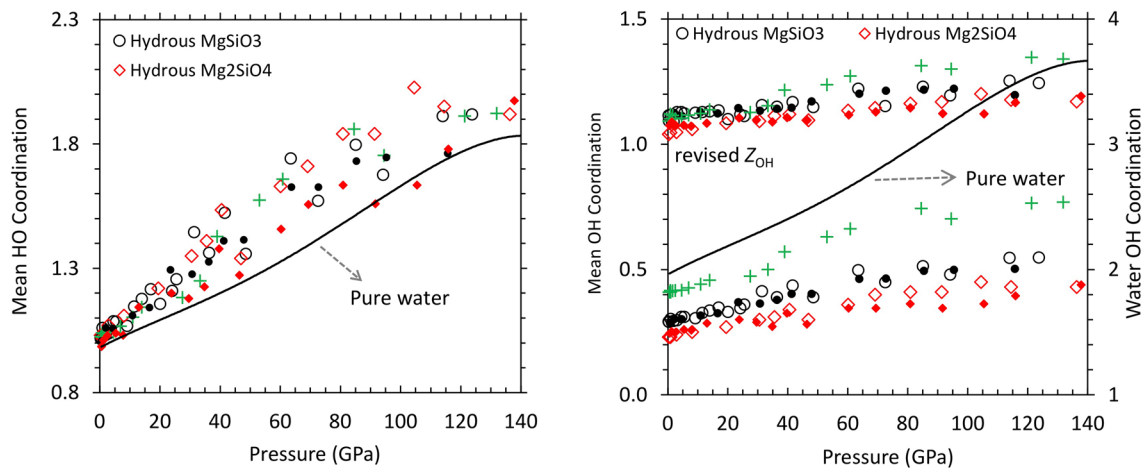


Figure 5. Mean H–O and O–H coordination numbers of hydrous MgSiO_3 with 8.2 wt% water (circles) and Mg_2SiO_4 with 6.0 wt% water (diamonds) and 11.4 wt% water (pluses) compared to those of pure water (solid black curve). The revised Z_{OH} (right) represents the mean coordination number evaluated by considering only oxygen atoms that contribute to the coordination. The results for the corresponding iron-bearing phases are shown by small solid symbols.

increasing pressure implying positive activation volume and all $\log D_{\text{H}}-P$ isotherms tend to be linear (Fig. 4). Comparison of these isotherms among different melts suggests that hydrogen diffuses somewhat faster in hydrous silicate melts with higher water content (Supplementary Fig. S3). The presence of iron tends to enhance hydrogen diffusion and diminish the differences in D_{H} between the two silicate melt systems (Supplementary Fig. S3). Oxygen diffuses much slower than hydrogen as expected (Fig. 4). At 2000 K, the $D_{\text{H}}/D_{\text{O}}$ ratio increases from ~4 to more than 10 over the pressure range 0–30 GPa. At 3000 K, this ratio exceeds 10 above 50 GPa and becomes so large at 80 GPa that O atoms (as well as Mg and Si atoms) can be essentially assumed as frozen with respect to H. At 4000 K, all atomic species including oxygen diffuse at discernable rates even at very high pressures. Our results thus suggest that hydrogen diffuses a few orders of magnitude faster than the host ions in silicate melts even at the conditions applicable to the deepest parts of the mantle.

In pure liquid water, hydrogen and oxygen diffuse in a different manner than in silicate melts. As pressure increases, both diffusivities (D_{H} and D_{O}) decrease rapidly almost overlapping with each other in low-pressure regime (Fig. 4), that is, the $D_{\text{H}}/D_{\text{O}}$ ratio remains close to 1 implying the diffusion of individual H_2O molecules at pressures up to 10 GPa. The simulated water is thus considered to be a molecular fluid at low pressures irrespective of temperature. As pressure increases further, hydrogen and oxygen diffusion decouple from each other. The D_{H} profile reaches a shallow minimum before it shows a gradual increasing trend at high pressures. On the other hand, the oxygen diffusivity continues to decrease with increasing pressure. The two diffusivity profiles systematically diverge with compression, for instance, the $D_{\text{H}}/D_{\text{O}}$ ratio is ~16 at 72 GPa (2000 K) and ~24 at 142 GPa (4000 K). Because hydrogen diffuses much faster than oxygen, the simulated water essentially represents a dissociated fluid state over much of the pressure regime studied.

We find that the calculated hydrogen and oxygen diffusivities of hydrous silicate melts are much smaller than those of the bulk water particularly at low temperatures (Fig. 4). Also, melt D_{H} and D_{O} differ from each other at all pressures, including zero pressure. Melt D_{H} decreases gradually with pressure with no anomalous behavior shown by water D_{H} . Melt D_{O} decreases monotonically with pressure though more rapidly than water D_{O} . In silicate melt, oxygen diffusion is also controlled by Mg–O and Si–O bond events. Our results show that the diffusivity isotherms of hydrous silicate melts and pure water differ more as pressure increases.

Speciation of hydrous component and structure of water. Hydrogen exclusively forms bond with oxygen in hydrous silicate melts as in bulk water. This is reflected by a sharp peak around 1 Å in the H–O radial distribution function and a broad peak in all other hydrogen-involved functions (Supplementary Fig. S4 and S5). So, the speciation of hydrous component in melts is determined by the local coordination environments of H and O. The calculated mean H–O coordination number (Z_{HO}) of hydrous silicate melts is slightly larger than 1 at zero pressure and its value increases almost linearly with pressure along each isotherm (Fig. 5, left). Melt Z_{HO} always remains above water Z_{HO} (which is 1 at zero pressure) with larger differences between them appearing at higher pressures. At zero pressure, we find that a small proportion (2–3%) of hydrogen atoms are coordinated with two oxygen atoms (that is, forming –O–H–O– bridge) in melts whereas all hydrogen atoms are singly oxygen-coordinated in water. The proportion of twofold and onefold coordination states increases and decreases, respectively, with increasing pressure more rapidly in melts compared to water (Supplementary Fig. S6). This difference arises partly because more oxygen atoms are available in hydrous melts than in pure water for hydrogen to form H–O bond. In the case of iron-bearing silicate melts, hydrogen has an affinity for iron, which is manifested by a shoulder-like feature in the H–Fe radial distribution function (Supplementary Fig. S4). The associated H–Fe bonding tends to cause a slight reduction in Z_{HO} .

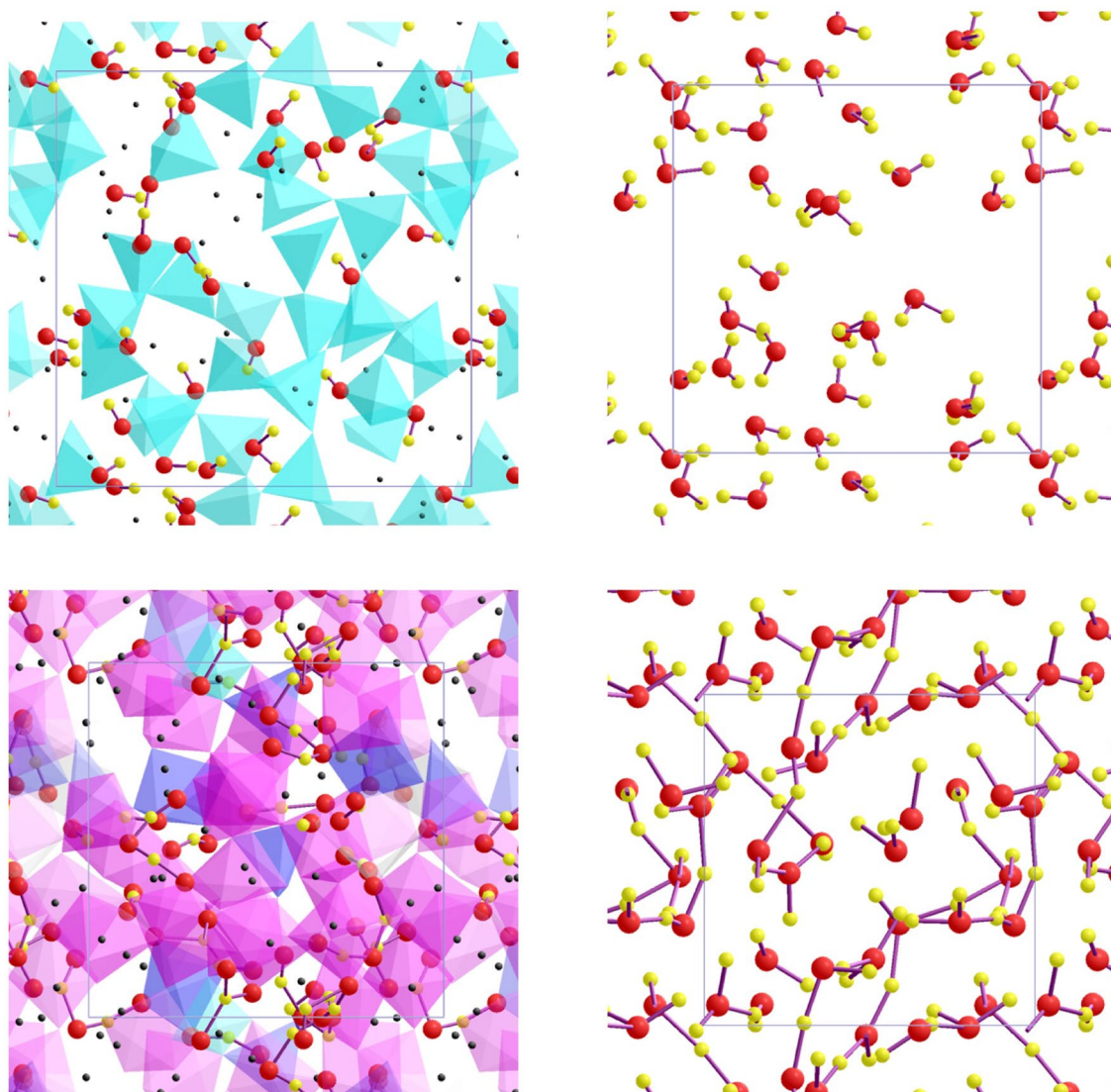


Figure 6. Visualization snapshots of hydrous silicate melt ($32 \text{ MgSiO}_3 + 16 \text{ H}_2\text{O}$) and bulk water ($24 \text{ H}_2\text{O}$) at low and high pressures⁶⁰. The hydrous melt consists of mostly hydroxyls with one H_2O molecule and one $-\text{O}-\text{H}-\text{O}-$ bridge at 0.2 GPa and 2000 K (top-left). It shows fewer hydroxyls, many $-\text{O}-\text{H}-\text{O}-$ bridges, and some longer sequences ($-\text{O}-\text{H}-\text{O}-\text{H}-\text{O}-$, $-\text{O}-\text{H}-\text{O}-\text{H}-\text{O}-\text{H}-\text{O}-$, HO_3) at 85.1 GPa and 3000 K (bottom-left). Also shown are the Si–O coordination states (cyan: tetrahedron, blue: pentahedron, magenta: octahedron) and Mg atoms (black dots). The simulated pure water contains only water molecules at 0.7 GPa and 2000 K (top-right). A highly compressed water (79.4 GPa and 3000 K) contains ten OH_2 , twelve OH_3 , and two OH_4 , which are also interconnected with each other via hydrogen (bottom-right).

On the other hand, the O–H coordination environment is sensitive to the Mg/Si ratio of melts. The calculated mean O–H coordination number (Z_{OH}) at zero pressure is 0.29 for hydrous MgSiO_3 melt and 0.23 for hydrous Mg_2SiO_4 melt. Its value increases with increasing pressure for both melts, and the differences between two melts persist at all pressures (Fig. 5, right). As expected, a large fraction of oxygen ($\sim 80\%$) in melts is not bonded with hydrogen. The rest of oxygen form mostly hydroxyls and some molecular water at low pressure (Fig. 6), generally consistent with the experimental observations^{48,49}. In contrast, every oxygen is bonded with two hydrogen atoms in water corresponding to $Z_{\text{OH}} = 2$ (and $Z_{\text{HO}} = 1$) and nearly 100% H_2O molecules at zero pressure (Fig. 6). On compression, oxygen is increasingly bonded with hydrogen in water and Z_{OH} exceeds 3 at high pressures. The proportion of H_2O molecules in water decreases rapidly as pressure increases (Supplementary Fig. S6), dropping to $\sim 85\%$ at 20 GPa, then to $\sim 50\%$ at 50 GPa and $\sim 10\%$ above 100 GPa. Larger groups, such as OH_3 , OH_4 and OH_5 all become increasingly abundant at higher pressure (Supplementary Fig. S6). Moreover, they are linked with each other to form more complex species as hydrogen is shared with two or even three oxygens because of space confinement at high pressures. A clear structural change thus occurs from a molecular liquid to a dissociated liquid (with larger OH_n groups and probably more ionic in nature) as the liquid water is compressed (Fig. 6). Two oxygen coordinated states of hydrogen (that is, $-\text{O}-\text{H}-\text{O}-$) facilitate hydrogen movement in both water and hydrous silicate melts. These hydrogen bridges act as transition state for hydrogen transfer from one

hydroxyl to another hydroxyl via the reaction $\text{O}-\text{H} + \text{O} = \text{O}-\text{H}-\text{O} = \text{O} + \text{H}-\text{O}$, where oxygen is also bonded with the other cation (Si or Mg in hydrous melts or hydrogen in the pure water).

Pressure systematically enhances the degree of oxygen–hydrogen bonding in hydrous silicate melts. Considering only oxygen atoms which are bonded with hydrogen, the revised value of Z_{OH} increases from ~ 1.1 to ~ 1.25 for hydrous MgSiO_3 melt and from ~ 1.05 to ~ 1.20 for hydrous Mg_2SiO_4 melt over the pressure ranges considered here (Fig. 5, right). The majority of oxygen (80–95%) are singly coordinated with hydrogen in silicate melts. The proportion of singly and doubly hydrogen-coordinated species (that is, hydroxyls and OH_2) gradually decreases and increases, respectively, with increasing pressure (Supplementary Fig. S6). Even hydronium group (OH_3) appears in discernable amounts (up to $\sim 3\%$) above 30 GPa. This pressure enhancement of twofold coordination states comprising of hydrogen and oxygen (that is, $-\text{O}-\text{H}-\text{O}-$ and $-\text{H}-\text{O}-\text{H}-$ groups) in silicate melts indicates a changing role of hydrogen from a network modifier at low pressure to a network former at high pressure (Fig. 6). The predicted pressure evolution of the hydrous speciation is generally consistent with previous computational studies of hydrous silicate melts^{6,7,24–26}.

Discussion and implications

Melt + water solution. The predicted negative volume of silicate melt + water solution at low pressures (for instance, -19 , -2.7 , and $-0.7 \text{ cm}^3 \text{ mol}^{-1}$, respectively, at 0.5, 5, and 10 GPa at 2000 K) can be attributed to the differences in local hydrogen–oxygen arrangement between silicate melt and pure water. The water component is dissolved in silicate melts primarily as hydroxyls and to some extent as molecular water, which are also bound to one or more cations via oxygen bonding (Fig. 6, left)). This means that the incorporation mechanism is predominantly chemical. On the other hand, the bulk water is in molecular liquid state exclusively consisting of loosely (physically) bound H_2O molecules at low pressures (Fig. 6, top-right)). Such a molecular fluid water is highly compressible, so its molar volume becomes comparable to the partial molar volume of the dissolved water of the melt at pressures above 15 GPa (Fig. 3). The pressure-induced similarity between two volumes can be associated with our finding that the H_2O component in melts as well as the bulk water become structurally well-connected (that is, exclusively chemical) at high compression. Enhanced participation of oxygen in hydrogen bonding becomes notable and also the proportions of species, such as H_3O and H_4O , are large in highly compressed bulk water, which represents the dissociation of water as in the case of hydrous melts. The system thus shows increasingly ideal volume of mixing with compression. This explains the experimental observations suggesting that water and silicate melt become completely miscible at high pressures⁴⁵. Our finding that hydrous melts of different compositions (varying Mg/Si and iron content) behave similarly at all pressures (Fig. 3) suggests that the predicted effects of hydration on melt properties are likely to be applicable to natural melt compositions as well.

Most previous first-principles computations used LDA to study silicate melts, including hydrous ones^{6,7,46,47}. Comparison of our new results with the previous results allow us to assess how much the evaluation of partial molar volume is sensitive to the choice of the exchange correlation functional (Supplementary Fig. S7). A general trend is that GGA gives systematically larger volume than LDA. This is indeed the case with both pure and hydrous silicate melts. The volume difference between GGA and LDA for these melts is large at zero pressure ($\sim 15\%$) and it decreases gradually with increasing pressure ($\sim 5\%$ at 50 GPa). This trend is also evident in the bulk water for which the volume difference is very large particularly at low pressures ($\sim 50\%$ at 0.5 GPa, $\sim 20\%$ at 5 GPa), dropping below 5% at pressures beyond 100 GPa. In the case of the partial molar volume of water, the GGA-LDA difference is large at low pressures but it almost vanishes at high pressures (Supplementary Fig. S7). As discussed earlier, our GGA prediction is expected to be more accurate than the previous LDA results in case of the molar volume of the dissolved water.

Density change by hydration. The water-induced reduction in the melt density tends to be nearly uniform with respect to pressure and temperature^{6,7,24}. The calculated density contrasts (Fig. 7) can be adequately described with the following relation:

$$\frac{\rho - \rho_0}{\rho_0} = [(-0.56 \pm 0.01) + (0.057 \pm 0.001)\ln(P)]x_m/100 \quad (4)$$

where ρ is the density of hydrous silicate melt, ρ_0 is the density of non-volatile component (dry silicate melt), and x_m is the mol percent of water in terms of oxide components. Our results are generally comparable with the previous estimates of the density contrasts based on the experimental data^{6,12} and first-principles simulations⁶ for more complex melt compositions (Fig. 7). These studies implied somewhat smaller density effects because they also inferred smaller partial molar volume of water dissolved in melts as discussed earlier (Fig. 2, left-inset). We find that the reduction in melt density by hydration depends linearly on water concentration. The density contrast varies gradually with pressure according to Eq. (4) (over much of the pressure regime except below 5 GPa), which is independent of temperature and melt composition within the computational uncertainty (Fig. 7, Supplementary Fig. S8). Our model differs from the previous model²⁴ which assumed that the density contrast only depends on water content in terms of weight percent. We find that the amount of water in terms of mol percent determines the magnitude of density contrast more accurately than that in terms of weight percent. This perhaps makes sense because the density changes are also related to the dilation caused by the hydrous component. If the melt + water solution has zero volume of mixing at all conditions, the density contrast between hydrous and anhydrous melts will vary rapidly initially and then gradually with pressure⁷. The predicted hydration density at low pressures is smaller than that in an ideal mixing case.

Silicate melts were prevalent in magma ocean environment soon after Earth was formed. Now they are present to much smaller extents, most likely in regions below mid-ocean ridges, regions above and below the mantle-transition region, and atop the core-mantle boundary. A melt formed just above the mantle transition

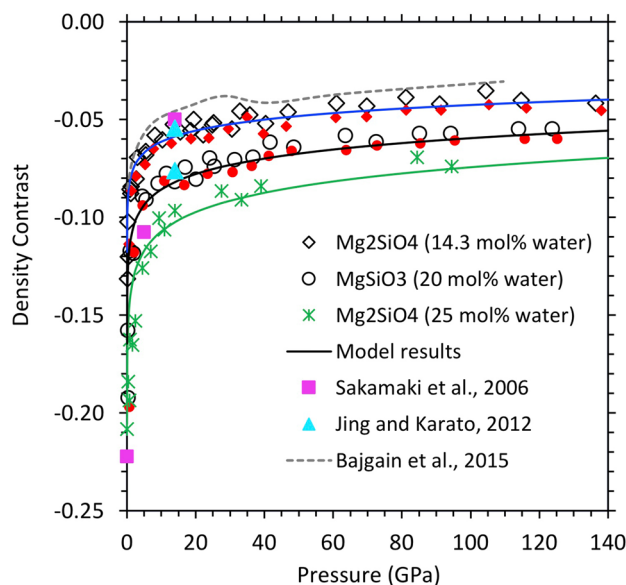


Figure 7. Density contrast between dry and hydrous melts for iron-free (open symbols and asterisks) and iron-bearing (filled small symbols) compositions as a function of pressure. The model results using Eq. 4 are shown by solid curves for the corresponding melt compositions. The previous results are shown for peridotite melt¹² containing ~20 mol% water at 0, 5, and 14 GPa at 1873 K (magenta squares), hydrous ultramafic melt³¹ with 20 and 25 mol% water at 14 GPa and 2173 K (cyan triangles), and hydrous model basalt⁶ with 13 mol% water along the 3000 K isotherm (dashed curve).

zone can be gravitationally stable if the melt density takes a value between the density of the upper mantle minerals near 410 km depth (3.54 g/cm^3) and the density of the materials at the top of mantle transition zone (3.73 g/cm^3). Using Eq. 4 with a density contrast evaluated⁵⁰ as $(3.54 - 3.73)/3.73 = -0.051$, we obtain $x_m = 12.4$ mol% at 14 GPa. This means that a melt containing up to 5 wt% water will be stable atop the mantle transition zone if the FeO content of melt is high (say, $\text{Fe}/(\text{Mg} + \text{Fe}) = 0.25$). Similarly, we estimate that up to 9 wt% water may be accommodated in a buoyantly neutral hydrous melt at the 660 km depth discontinuity corresponding to its large density jump⁵⁰ of 0.38 g/cm^3 . The implied presence of gravitationally trapped hydrous partial melts at these depths have been previously suggested^{6,12,26,51}. The water content of possible melts at these depths also depends on the iron content because water and iron change the density in an opposite way. Both iron and water are preferably partitioned into melts when partial melting occurs at a depth or when a magma ocean starts to crystallize resulting in a dense hydrous melt.

Electrical conductivity. Highly mobile hydrogen ions carrying positive charges (as protons) can contribute to the electrical conductivity (σ) of melts. We evaluate this contribution from the calculated diffusivity (D) values (Fig. 4) using the Nernst-Einstein relation as previously done⁷

$$\sigma = \frac{Dnq^2}{kTH_R} \quad (5)$$

where n is the number density of mobile carriers with electrical charge q , and k denotes the Boltzmann constant. The Haven ratio H_R is a correlation factor for the ionic motion and approaches one for small n , so we take $H_R = 1$. For hydrous silicate melts, we consider protons (H^+ ions) as the primary charge carriers; $q = +1e$. Our results show that the hydrogen-induced (ionic) conductivity of hydrous silicate melts (σ_{melt}) takes larger value at higher temperature, but along each isotherm it remains almost constant with respect to pressure (Fig. 8; Supplementary Fig. S9). The average conductivity over the pressure ranges considered here corresponds to 100, 247, and 480 S/m, respectively, at 2000, 3000, and 4000 K for (Mg,Fe)SiO₃ melts with 20.0 mol% water. The corresponding σ_{melt} values of hydrous (Mg,Fe)₂SiO₄ melts are 63, 160, and 293 S/m for 14.3 mol% water and 138, 328, and 597 S/m for 25.0 mol% water. As expected, hydrous melt becomes more conductive for higher water concentration. These average conductivity values can be described by the following concentration-dependent Arrhenius model:

$$\sigma(x_m, T) = \sigma_0(x_m) \exp[-E/(RT)] \quad (6)$$

where $\sigma_0(x_m) = -435 + 12150x_m$ is the pre-exponential factor, varying linearly with the mol percent of water (x_m), and $E = 50 \pm 2 \text{ kJ/mol}$ is the activation energy which is independent of water content. The model predicts a value of 43 S/m at 1873 K and 14 GPa, which compares well with the experimentally inferred value⁸ of 37 S/m.

In pure water, hydrogen diffuses primarily as neutral H₂O molecules at low pressure. We exclude the hydrogen atoms of molecular water by approximating the effective concentration of charge carriers by $(1-f)n$, where f is the proportion of H₂O species. The estimated electrical conductivity of bulk water (σ_{water}) increases rapidly initially and then gradually as pressure increases (Fig. 8). Our results compare favorably with previous computational

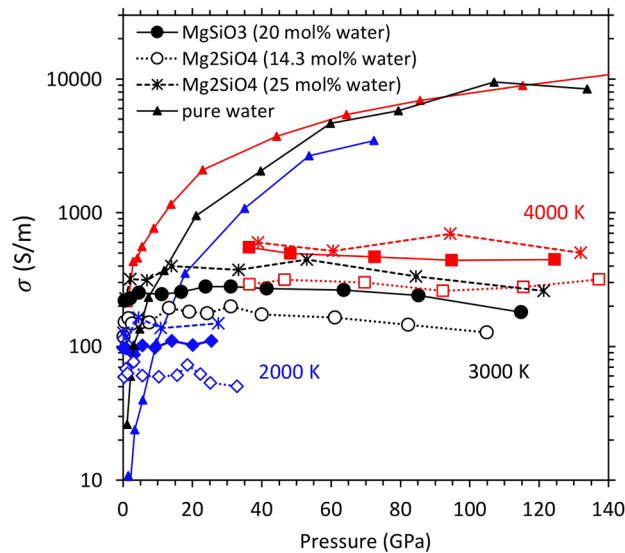


Figure 8. Hydrogen-induced electrical conductivity (σ) of hydrous MgSiO_3 (filled symbols) and Mg_2SiO_4 melts (open symbols and asterisks) and bulk water (solid curves) as a function of pressure at different temperatures as shown. The melt conductivity at 3000 and 4000 K represent the averages taken between the iron-free and iron-bearing compositions (iron has almost no influence on the conductivity, Supplementary Fig. S9). The errors in the calculated electrical conductivity lie within 20%.

results^{30,52} and measured shock wave data^{53,54}. The predicted pressure behavior represents ionic conduction as water upon compression changes from an insulating molecular liquid to a fully dissociated ionic liquid. Highly compressed water behaves as a superionic liquid in which oxygen ions essentially become frozen compared to highly mobile hydrogen ions (D_{O} is one to two orders of magnitude smaller than D_{H} as shown in Fig. 4). We find that σ_{water} is smaller than σ_{melt} at pressures up to 10 GPa when pure water behaves as a molecular fluid (Fig. 8). As the water is compressed further, σ_{water} exceeds σ_{melt} because hydrogen ion diffuses via O–H bond breaking/formation events. Both the concentration and diffusion rate of charge carriers (H^+) in compressed bulk water are high compared to those in hydrous silicate melts.

We estimate the electrical conductivity of a gravitationally stable partial melt layer at 410 km depth containing 5 wt% water as discussed above. This corresponds to $x_{\text{m}} \sim 13$ mol% for which using Eq. 6 gives $\sigma_{\text{melt}} = 39$ S/m at 1800 K. So, a partial melt layer containing a few percent (say, 3 volume %) of hydrous melt corresponds to a high conductivity of ~ 0.8 S/m using the Hashin–Shtrikman scheme with the assumption that the electrical conductivity of solid grains is negligible (Supplementary text 2). Electrical conductivities in the range 0.1 to 2.0 S/m have been reported in the upper-mantle-transition regions by electromagnetic sounding observations^{16–18}.

Summary. In most cases, silicate melts contain some water. Whether such hydrous melt sinks or rises or stagnates at a depth controls the amount of water that may be entertained in the interior and its subsequent contributions to global water cycle at all times of Earth's history. For instance, upwelling hydrous magmas may have been contributing to the origin and maintenance of the atmosphere and hydrosphere. To better understand these issues requires a full knowledge about the behavior and properties of hydrous silicate melts at relevant pressure and temperature conditions. This study represents a major progress in this endeavor as it reports the results of first-principles molecular dynamics simulations of hydrous silicate melts covering wide ranges of pressure (up to 140 GPa), temperature (2000 to 4000 K), and composition (water content, Mg/Si ratio, iron content). Using the simulation results, we have made quantitative evaluation of the effects of water on the density and electrical conductivity of silicate melts. These effects are further linked to the thermodynamic and structural differences between water in silicate melts and water in its bulk (pure) form. The water component is less compressible than bulk water, particularly at low pressures. Water is dissolved in melts in dissociated form mostly as hydroxyls at low pressure and as extended species on further compression. Bulk water behaves differently as it changes from a fully molecular fluid to a dissociated fluid with compression. As a consequence, the volume of silicate melt + water solution is non-ideal at low pressure and becomes zero above 15 GPa, irrespective of melt composition and water concentration. Also, hydrogen diffusion is decoupled from the rest of ions including oxygen in silicate melts and the associated highly mobile protons make substantial contributions to electrical conduction. Finally, we have demonstrated that the water component controls the stability and conductance of partial melts in the mantle.

Methods

First-principles molecular dynamics simulations of several silicate melt + water systems were performed using the generalized gradients approximation (PBE exchange–correlation functional)⁵⁵ and project augmented wave method⁵⁶ as implemented in VASP⁵⁷. All simulations were based on canonical NVT ensembles where the number of atoms N , volume V , and temperature T are fixed. The supercells consisted of $32\text{MgSiO}_3 + 16\text{H}_2\text{O}$ ($N=208$), $16\text{Mg}_2\text{SiO}_4 + 8\text{H}_2\text{O}$ ($N=136$), and $16\text{Mg}_2\text{SiO}_4 + 16\text{H}_2\text{O}$ ($N=160$) for hydrous silicate melts containing 8.2, 6.0, and 11.4 wt% water (equivalently, 20.0, 14.3 and 25.0 mol% water), respectively. The corresponding water-free supercells involved 32MgSiO_3 and $16\text{Mg}_2\text{SiO}_4$. To simulate iron-bearing melts, Mg atoms were substituted with Fe atoms for $x = \text{Fe}/(\text{Mg} + \text{Fe}) = 0.25$. A plane wave cutoff of 400 eV and Gamma Point Brillouin zone sampling were used. Pulay stress added to the calculated pressure varies between ~ 3 and ~ 8 GPa over the volume range $V/V_0 = \sim 1.0$ to ~ 0.4 (where V_0 is the zero-pressure volume shown in Table 1) considered in this study.

The input configurations for each melt composition at different volumes were generated at temperatures well above the melting point followed by quenching to desired lower temperatures of 4000, 3000, and 2000 K. The run duration varies between 20 and 80 picoseconds with a time step of 1 femtosecond depending on volume and temperature. The liquid state was confirmed in each case by assuring that the radial distribution functions show no long-range order and the mean square displacement functions show diffusive regime⁵⁸. We also performed a few simulations using the local density approximation⁵⁹. The calculated results were assured to be adequately converged with respect to run duration, time step, and supercell size by performing additional simulations at selected conditions. For comparisons, pure fluid water was simulated using 24 formula units ($N=72$), a plane wave cutoff of 600 eV, and a timesetp of 0.5 femtosecond. The applied Pulay stress varies from 0.2 to 0.8 GPa over the sixfold compression regime considered. Further details about the simulation and data analysis methods can be found in previous publications^{6,25,58}

Received: 22 February 2021; Accepted: 6 May 2021

Published online: 19 May 2021

References

- Hirschmann, M. M. Water, melting, and the deep Earth H_2O cycle. *Rev. Earth Planet. Sci.* **34**, 629–653 (2006).
- Schmandt, B., Jacobsen, S. D., Becker, T. W., Liu, Z. & Dueker, K. G. Dehydration melting at the top of the lower mantle. *Nature* **344**, 1265–1268 (2014).
- Karato, S.-I., Karki, B. B. & Park, J. Deep mantle melting, global water circulations and its implications for the stability of the ocean mass. *Prog. Earth Planet. Sci.* **7**, 76 (2020).
- Matsukage, K. N., Jing, Z. & Karato, S. Density of hydrous silicate melt at the conditions of Earth's deep upper mantle. *Nature* **438**, 488–491 (2005).
- Sakamaki, T., Ohtani, E., Urakawa, S., Suzuki, A. & Katayama, Y. Measurement of hydrous peridotite magma density at high pressure by X-ray absorption method. *Earth Planet. Sci. Lett.* **287**, 293–297 (2009).
- Bajgain, S., Ghosh, D. B. & Karki, B. B. Structure and density of basaltic melts at mantle conditions from first-principles simulations. *Nature Comm.* **6**, 8578 (2015).
- Mookherjee, M., Stixrude, L. & Karki, B. B. Hydrous silicate melt at high pressure. *Nature* **452**, 983–986 (2008).
- Ni, H., Keppler, H. & Behrens, H. Electrical conductivity of hydrous basaltic melts: implications for partial melting in the upper mantle. *Contrib. Mineral. Petrol.* **162**, 637–650 (2011).
- Freitas, D. & Manthilake, G. Electrical conductivity of hydrous silicate melts: Implications for the bottom-up hydration of Earth's upper mantle. *Earth Planet. Sci. Lett.* **523**, 115712 (2019).
- Sakamaki, T. Density of hydrous magma. *Chem. Geol.* **475**, 135–139 (2017).
- Dufils, T., Sator, N. & Guillot, B. A comprehensive molecular dynamics simulation of hydrous magmatic liquids. *Chem. Geol.* **533**, 119300 (2020).
- Sakamaki, T., Suzuki, A. & Ohtani, E. Stability of hydrous melt at the base of the Earth's upper mantle. *Nature* **439**, 192–194 (2006).
- Karki, B. B., Ghosh, D. B., Maharjan, C., Karato, S.-I. & Park, J. Density-pressure profiles of Fe-bearing MgSiO_3 liquid: Effects of valence and spin states, and implications for the chemical evolution of the lower mantle. *Geophys. Res. Lett.* **45**, 3959–3966 (2018).
- Agee, C. B. Compressibility of water in magma and the prediction of density crossovers in mantle differentiation. *Philos. Trans. R. Soc.* **366**, 4239–4252 (2008).
- Stixrude, L., De Koker, N., Sun, N., Mookherjee, M. & Karki, B. B. Thermodynamics of silicate liquids in the deep Earth. *Earth Planet. Sci. Lett.* **278**, 226–232 (2009).
- Lizarralde, D., Chave, A., Hirth, G. & Schultz, A. Northeastern Pacific mantle conductivity profile from long-period magnetotelluric sounding using Hawaii-to-California submarine cable data. *J. Geophys. Res.* **100**, 17837–17854 (1995).
- Toffelmier, D. A. & Tyburczy, J. A. Electromagnetic detection of a 410-km-deep melt layer in the southwestern United States. *Nature* **447**, 991–994 (2007).
- Baba, K. *et al.* Electrical conductivity imaging of the Phillipine Sea upper mantle using seafloor magnetotelluric data. *Phys. Earth Planet. Inter.* **183**, 44–62 (2010).
- Manning, C. E. The influence of pressure on the properties and origins of hydrous silicate liquids in Earth's interior. In: Kono, Y., Sanloup, C. (Eds.), *Magmas Under Pressure: Advances in High-Pressure Experiments on Structure and Properties of Melts*, Cambridge, 83–114 (2018).
- Ochs, F. A. & Lange, R. A. The density of hydrous magmatic liquids. *Science* **283**, 1314–1317 (1999).
- Bouhifd, M. A., Whittington, A. & Richet, P. Densities and volumes of hydrous silicate melts: new measurements and predictions. *Chem. Geol.* **418**, 40–50 (2015).
- Gaillard, F. Laboratory measurements of electrical conductivity of hydrous and dry silicic melts under pressure. *Earth Planet. Sci. Lett.* **218**, 215–228 (2004).
- Guo, X., Bin, L., Ni, H. & Mao, Z. Electrical conductivity of hydrous andesitic melts pertinent to subduction zones. *J. Geophys. Res. Solid Earth* **122**, 1777–1788 (2017).
- Du, Z. *et al.* Fate of hydrous Fe-rich silicate melt in Earth's deep mantle. *Geophys. Res. Lett.* **46**, 9466–9473 (2019).
- Karki, B. B., Ghosh, D. & Banjara, D. Mixed incorporation of carbon and hydrogen in silicate melts under varying pressure and redox conditions. *Earth Planet. Sci. Lett.* **549**, 116520 (2020).
- Yuan, L., Steinle-Neumann, G. & Suzuki, A. Structure and density of H_2O -rich Mg_2SiO_4 melts at high pressure from ab initio simulations. *J. Geophys. Res. Solid Earth* **125**, e2020JB020365 (2020).

27. Encrenaz, T. Water in the solar system. *Annu. Rev. Astron. and Astrophys.* **46**, 57–87 (2008).
28. Baraffe, I., Chabrier, G. & Barman, T. The physical properties of extra-solar planets. *Rep. Prog. Phys.* **73**, 016901 (2010).
29. Millot, M. *et al.* Nanosecond X-ray diffraction of shock-compressed superionic water ice. *Nature* **569**, 251–255 (2019).
30. Mattsson, T. R. & Desjarlais, M. P. Phase diagram and electrical conductivity of high energy density water from density functional theory. *Phys. Rev. Lett.* **97**, 017801 (2006).
31. Jing, Z. & Karato, S. Effect of H₂O on the density of silicate melts at high pressures: static experiments and the application of a modified hard-sphere model of equation of state. *Geochim. Cosmochim. Acta* **85**, 357–372 (2012).
32. French, M., Mattsson, T. R., Nettelmann, N. & Redmer, R. Equation of state and phase diagram of water at ultrahigh pressures as in planetary interiors. *Phys. Rev. B* **79**, 054107 (2009).
33. Pitzer, K. S. & Sterner, S. M. Equations of state valid continuously from zero to extreme pressures for H₂O and CO₂. *J. Chem. Phys.* **101**, 3111–3116 (1994).
34. Withers, A. C., Kohn, S. C., Brooker, R. A. & Wood, B. J. A new method for determining the P-V-T properties of high-density H₂O using NMR: results at 1.4–4.0 GPa and 700–11°C. *Geochim. Cosmochim. Acta* **64**, 1051–1057 (2000).
35. Sanchez-Valle, C., Mantegazzi, D., Bass, J. D. & Reusser, E. Equation of state, refractive index and polarizability of compressed water to 7 GPa and 673 K. *J. Chem. Phys.* **138**, 054505 (2013).
36. Sugimura, E. *et al.* Compression of H₂O ice to 126 GPa and implications for hydrogen bond symmetrization: Synchrotron x-ray diffraction measurements and density functional calculations. *Phys. Rev. B* **77**, 214103 (2008).
37. Ochs, F. A. & Lange, R. A. The partial molar volume, thermal expansivity, and compressibility of H₂O in NaAlSi₃O₈ liquid: new measurements and an internally consistent model. *Contrib. Mineral. Petrol.* **142**, 235–243 (1997).
38. Makhluaf, A. R., Newton, R. C. & Manning, C. E. Hydrous albite magmas at lower crustal pressure: new results on liquidus H₂O content, solubility, and H₂O activity in the system NaAlSi₃O₈-H₂O-NaCl at 1.0 GPa. *Contrib. Mineral. Petrol.* **171**, 75 (2016).
39. Malfait, W. J., Seifert, R., Petitgirard, S., Mezouar, M. & Sanchez-Valle, C. The density of andesitic melts and the compressibility of dissolved water in silicate melts at crustal and upper mantle conditions. *Earth Planet. Sci. Lett.* **393**, 31–38 (2014).
40. Malfait, W. J. *et al.* Supervolcano eruptions driven by melt buoyancy in large silicic magma chambers. *Nat. Geosci.* **7**, 122–125 (2014).
41. Agee, C. B. Static compression of hydrous silicate melt and the effect of water on planetary differentiation. *Earth Planet. Sci. Lett.* **265**, 641–654 (2008).
42. Seifert, R., Malfait, W. J., Petitgirard, S. & Sanchez-Valle, C. Density of phonolitic magmas and time scales of crystal fraction in magma chambers. *Earth Planet. Sci. Lett.* **381**, 12–20 (2013).
43. Bureau, H. & Keppler, H. Complete miscibility between silicate melts and hydrous fluids in the upper mantle: experimental evidence and geochemical implications. *Earth Planet. Sci. Lett.* **165**, 187–196 (1999).
44. Papale, P., Moretti, R. & Barbato, D. The compositional dependence of the saturation surface of H₂O + CO₂ fluids in silicate melts. *Chem. Geol.* **229**, 78–95 (2006).
45. Mibe, K. *et al.* Second critical endpoint in the peridotite-H₂O system. *J. Geophys. Res. Solid Earth* **112**, B03201 (2007).
46. Karki, B. B., Bhattarai, D., Mookherjee, M. & Stixrude, L. Visualization-based analysis of structural and dynamical properties of simulated hydrous silicate melt. *Phys. Chem. Mineral.* **37**, 103–117 (2010).
47. Karki, B. B. & Stixrude, L. First-principles study of enhancement of transport properties of silica melt by water. *Phys. Rev. Lett.* **104**, 744–751 (2010).
48. Stolper, E. The speciation of water in silicate melts. *Geochim. Cosmochim. Acta* **46**, 2609–2620 (1982).
49. Behrens, H. Water speciation in oxide glasses and melts. *Chem. Geo.* **558**, 119850 (2020).
50. Dziewonski, A. M. & Anderson, D. L. Preliminary reference Earth model. *Phys. Earth Planet. Inter.* **25**, 297–356 (1981).
51. Fei, H. Water content of the dehydration melting layer in the topmost lower mantle. *Geophys. Res. Lett.* **48**, e2020GL090973 (2021).
52. French, M., Mattsson, T. R. & Redmer, R. Diffusion and electrical conductivity in water at ultrahigh pressures. *Phys. Rev. B* **82**, 174108 (2010).
53. Mitchell, A. C. & Nellis, W. J. Equation of state and electrical conductivity of water and ammonia shocked to the 100 GPa (1 Mbar). *J. Chem. Phys.* **76**, 6273 (1982).
54. Chau, R., Mitchell, A. C., Minich, R. W. & Nellis, W. J. Electrical conductivity of water compressed dynamically to pressures of 70–180 GPa (0.7–1.8 Mbar). *J. Chem. Phys.* **114**, 1361–1365 (2001).
55. Perdew, J. P., Burke, K. & Ernzerhof, M. Generalized gradient approximation made simple. *Phys. Rev. Lett.* **77**, 3865–3868 (1996).
56. Kresse, G. & Joubert, D. From ultrasoft pseudopotentials to the projector augmented-wave method. *Phys. Rev. B* **59**, 1758–1975 (1999).
57. Kresse, G. & Furthmüller, J. Efficiency of ab-initio total energy calculations for metals and semiconductors using a plane-wave basis set. *Comp. Mater. Sci.* **6**, 15–50 (1996).
58. Karki, B.B., Ghosh, D.B. & Bajgain, S.K. Simulation of silicate melts under pressure. In: Kono, Y. & Sanloup, C. (Eds.), *Magmas Under Pressure: Advances in High-Pressure Experiments on Structure and Properties of Melts*, pp. 419–453, Elsevier. (2018b).
59. Ceperley, D. M. & Alder, B. J. Ground-state of the electron-gas by a stochastic method. *Phys. Rev. Lett.* **45**, 566–569 (1980).
60. Bhattarai, D. & Karki, B. B. Atomistic visualization: space-time multiresolution integration of data analysis and rendering. *J. Mol. Graph Model* **27**, 951–968 (2009).

Acknowledgements

This work was supported by National Science Foundation (EAR 1764140, EAR 2001074, and EAR 2001339). The computing resources provided by Louisiana State University High Performance Computing.

Author contributions

B.B.K. designed research and performed simulations. All authors contributed to the analysis and discussion of the results, and to the preparation of the manuscript.

Competing interests

The authors declare no competing interests.

Additional information

Supplementary Information The online version contains supplementary material available at <https://doi.org/10.1038/s41598-021-90124-7>.

Correspondence and requests for materials should be addressed to B.B.K.

Reprints and permissions information is available at www.nature.com/reprints.

Publisher's note Springer Nature remains neutral with regard to jurisdictional claims in published maps and institutional affiliations.



Open Access This article is licensed under a Creative Commons Attribution 4.0 International License, which permits use, sharing, adaptation, distribution and reproduction in any medium or format, as long as you give appropriate credit to the original author(s) and the source, provide a link to the Creative Commons licence, and indicate if changes were made. The images or other third party material in this article are included in the article's Creative Commons licence, unless indicated otherwise in a credit line to the material. If material is not included in the article's Creative Commons licence and your intended use is not permitted by statutory regulation or exceeds the permitted use, you will need to obtain permission directly from the copyright holder. To view a copy of this licence, visit <http://creativecommons.org/licenses/by/4.0/>.

© The Author(s) 2021